ELSEVIER

Contents lists available at ScienceDirect

Case Studies in Construction Materials

journal homepage: www.elsevier.com/locate/cscm





Axial compressive performance of concrete-filled UHPC tubular columns reinforced with self-prestressed Fe-SMA spiral stirrups

Chushi Cui ^{a,b}, Zhiqiang Dong ^{a,b,*}, Yifan Zhao ^c, Tianhao Han ^{a,b}, Yichuan Zheng ^{a,b}, Yijie Pan ^d, Elyas Ghafoori ^e

- ^a Key Laboratory of Concrete and Prestressed Concrete Structures of Ministry of Education, Southeast University, Nanjing 211189, China
- b National and Local Joint Engineering Research Center for Intelligent Construction and Maintenance, Southeast University, Nanjing 211189, China
- ^c Department of Civil and Environmental Engineering, Hong Kong Polytechnic University, Hung Hom, Kowloon 999077, Hong Kong
- ^d Fusteel Co., Ltd., Huzhou 313011, China
- e Faculty of Civil engineering and Geodetic Science, Institute for Steel Construction, Leibniz University Hannover, Hannover 30167, Germany

ARTICLE INFO

Keywords:

Iron-based shape memory alloy (Fe-SMA) Ultra-high performance concrete (UHPC) Self-prestressing Concrete-filled UHPC tube Axial compression behavior Active confinement

ABSTRACT

This study investigates the axial compressive behavior of an innovative composite column comprising a prefabricated ultra-high performance concrete (UHPC) tube reinforced with selfprestressed iron-based shape memory alloy (Fe-SMA) spiral stirrups and cast-in-place ordinary concrete. Embedding Fe-SMA spirals within UHPC tubes during autoclave curing simultaneously activates the self-prestressing effect, enhancing UHPC's mechanical properties and imposing active circumferential confinement. Experimental tests were conducted on 24 specimens to evaluate the effects of Fe-SMA prestress levels, stirrup spacing, and curing methods. Results revealed that the self-prestressed Fe-SMA reinforced composite columns exhibited superior axial load-bearing capacity (up to 3694 kN), elastic modulus and ductility compared to non-prestressed counterparts. The self-prestressed Fe-SMA spirals effectively mitigate the inherent brittleness of UHPC, delay crack propagation, and promote strain-softening behavior. Compared to nonprestressed Fe-SMA-confined specimens, the compressive deformation capacity and hoop stiffness are improved by 28.15 % and 15.77 %, respectively. Notably, reducing Fe-SMA stirrup spacing effectively enhances confinement efficiency, while autoclave curing improves compressive strength by 17-31 % over natural curing. A calculation method is proposed to predict the ultimate load-bearing capacity of the composite columns, which closely matches experimental results, with errors below 10 %. This research validates the feasibility of the proposed composite system, offering a cost-effective and durable solution for prefabricated structural columns in marine and cross-sea bridge engineering.

1. Introduction

In modern civil engineering, conventional concrete increasingly struggles to satisfy the demanding performance requirements of marine floating structures, cross-sea bridges, and high-rise buildings in terms of load-bearing capacity, durability, and construction efficiency [1–3]. Ultra-high performance concrete (UHPC), as an advanced cementitious material [4,5], has emerged as a promising

E-mail address: zhiqiang.dong@seu.edu.cn (Z. Dong).

^{*} Corresponding author at: Key Laboratory of Concrete and Prestressed Concrete Structures of Ministry of Education, Southeast University, Nanjing 211189, China.

solution for these applications due to its exceptional compressive strength, superior durability, and remarkable toughness [6,7]. However, the widespread adoption of UHPC in full-scale structures remains constrained by its production costs, which are 6–8 times higher than those of conventional concrete [8]. A more cost-effective approach is using UHPC in critical structural components, forming UHPC-concrete composite systems. This hybrid approach optimizes material utilization by combining the performance advantages of UHPC with the economic benefits of ordinary concrete [9,10].

In recent years, research on concrete-filled UHPC tube (CFUT) has gained significant attention [11-14] owing to its notable advantages: (1) The prefabricated UHPC tube serves as both permanent formwork and structural component, synergistically interacting with the infill concrete to enhance load-bearing capacity [15]; (2) The exceptional durability of UHPC provides effective protection for the internal ordinary concrete, reducing the maintenance costs for cover associated with environmental exposure [16-18]; (3) Experimental studies have demonstrated superior bond performance between UHPC and conventional concrete, which ensures structural integrity [19-21]. Tian et al. [8.15] systematically investigated the axial compression and seismic performance of CFUT columns, revealing significant improvements in load capacity, deformation capability, and ductility compared to conventional RC columns. Ding et al. [9] experimentally investigated the axial compression behavior of CFUT columns reinforced with FRP stirrups, revealing that the UHPC tube exhibited minimal spalling during compression, with effective collaboration between the UHPC tube and the infill concrete, while reducing stirrup spacing significantly enhanced the ductility of the specimens. Xiong et al. [22] investigated the axial compression behavior of concrete-filled prefabricated aligned steel fiber UHPC tubes, the findings indicated the specimens exhibited remarkable improvements across various metrics than the ordinary concrete columns. However, CFUT columns face several challenges: the crucial curing conditions required for UHPC [4,23] are difficult to achieve in certain construction environments lacking adequate thermal curing facilities [24]. Furthermore, under compression, the UHPC tube may laterally expand and crack, which reduces its resistance to chloride ion penetration [25–27]. Chloride ions can infiltrate through these cracks, accelerating the corrosion of the internal reinforcement [28,29], thereby jeopardizing the safety and service life of the structural elements.

Although the current application of FRP or conventional steel stirrups to confine concrete [30] has a positive strengthening effect, this confinement method is only effective when dilation of the columns occurs due to axial loading, so it is called passive confinement [31,32]. There are several problems associated with passive confinement, including low material utilization, uncoordinated deformation between FRP or conventional steel stirrups and concrete, susceptibility to brittle failure, and stress hysteresis [33,34]. According to research [35], only 20 %–30 % of the strength of FRPs can be utilized when used in passively confined concrete columns. Given the above disadvantages of passive confinement, researchers have proposed a strengthening method known as active confinement using prestressed materials [36,37]. In the case of active confinement, lateral pressure is applied to the columns before loading to achieve synergy between the concrete columns and the confining materials, and this approach can also prevent stress hysteresis [38,39]. Additionally, active confinement can reduce the initial damage to concrete columns, improve material utilization, and fully utilize the strength of the confining materials [40,41].

However, traditional prestressing techniques in new structures, such as pre-tensioning or post-tensioning, face significant limitations when applied to thin-walled or curved concrete structures, including the need for large anchoring devices at the ends, frictional losses in curved configurations, and substantial space requirements during tensioning [42–45]. These constraints make them unsuitable for UHPC tubes. In recent years, iron-based shape memory alloys (Fe-SMAs) have emerged as a promising solution to

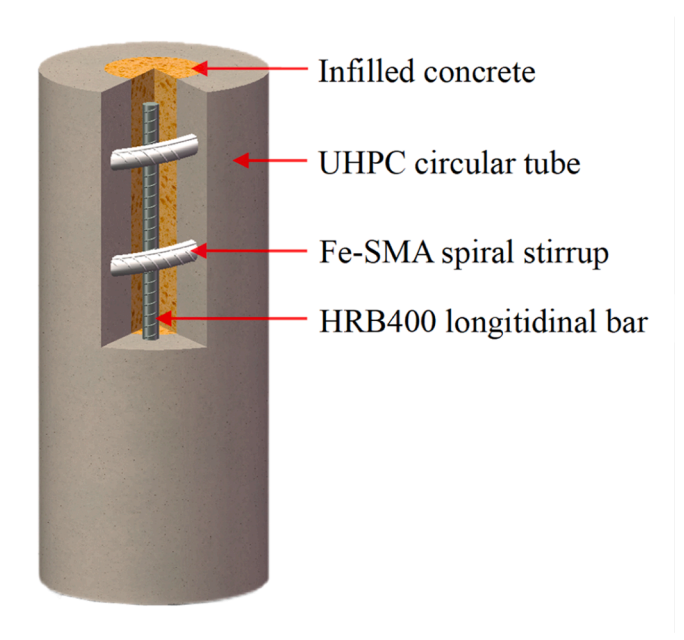


Fig. 1. The schematic diagram of concrete-filled UHPC tubular column reinforced with Fe-SMA spiral stirrups.

overcome the limitations of traditional prestressing methods [46–50]. Fe-SMAs, composed primarily of iron, nickel, titanium and manganese, offer distinct advantages such as cost-effectiveness, superior corrosion resistance, and a high elastic modulus [51–55]. Their unique shape memory effect allows them to recover their original shape upon heating, thereby automatically applying prestress to concrete structures [56–58]. Recent studies have demonstrated the effectiveness of Fe-SMA in improving the tensile performance and crack resistance of concrete structures [44,59,60]. For instance, Ji et al. [61] investigated the feasibility of using Fe-SMA rebar as cracking resistance spiral stirrup in the anchorage zone of prestressed concrete columns, experimental results revealed that the active circumferential confinement provided by Fe-SMA spirals effectively mitigated internal cracking in the anchorage zone and enhanced crack resistance. Dong et al. [44] experimentally studied the use of Fe-SMA wires to improve the crack resistance of UHPC members. Their findings indicated that when heated to 150 °C, Fe-SMA-reinforced specimens exhibited average crack resistance loads 13.4 % and 9.8 % higher than those of unreinforced and steel wire-reinforced specimens, respectively, demonstrating the feasibility of activating Fe-SMA to generate prestress and improve crack resistance.

Building on this, this paper innovatively proposes a self-prestressed Fe-SMA spiral stirrup-reinforced UHPC tube, as shown in Fig. 1. The prefabricated Fe-SMA-reinforced UHPC tube can serve as a permanent formwork for cast-in-place concrete, eliminating the need for traditional formwork. By employing "autoclave curing", this method simultaneously achieves effective short-term curing of UHPC and activates the Fe-SMA spiral stirrups to provide circumferential prestress [62–64]. Research by Chen et al. [65] has demonstrated that autoclave curing is one of the most effective curing methods for UHPC. The high-pressure environment during this process promotes the transformation of C-S-H (calcium silicate hydrate) gels into tobermorite within the UHPC matrix, filling internal pores, reducing harmful voids, and enhancing the density and overall properties of UHPC. Additionally, the high-temperature environment during autoclave curing activates the shape memory effect of Fe-SMA, applying circumferential compressive stress to the UHPC tube [68], thereby enhancing its crack resistance and achieving a dual-purpose outcome. With an autoclave curing of approximately 2–3 h, the proposed Fe-SMA-reinforced UHPC tubes are ideally suited for factory prefabrication, serving as stay-in-place formworks for cast-in-place concrete [15,69].

In summary, a novel composite form of concrete-filled UHPC tubular column reinforced with self-prestressed Fe-SMA spiral stirrup is proposed in this paper. The prefabricated Fe-SMA-reinforced UHPC tube serves as a permanent formwork for cast-in-place concrete, fully utilizing the high compressive strength and durability of UHPC, while the circumferential prestress provided by Fe-SMA enhances the specimen's resistance to lateral expansion. A total of 24 composite columns, each with a diameter of 200 mm and a height of 500 mm, were cast to investigate the effects of prestressing, Fe-SMA spiral spacing, and curing methods on axial compression performance. Furthermore, a calculation method for the load-bearing capacity of the composite columns was developed and validated against experimental results. This study aims to explore the feasibility of the proposed composite form, paving the way for its broader application in marine infrastructure, cross-sea bridges, and other demanding engineering fields.

2. Material properties

2.1. Fe-SMA rebars

The Fe-SMA used in this study is shown in Fig. 2. The Fe-SMA rebars are acid-pickled, hot-rolled, and ribbed, with a nominal diameter of 10 mm. The first batch of industrially produced Fe-SMA rebars in China have stable recovery stress performance. Table 1 presents the mechanical parameters of Fe-SMA rebars used in this study compared to HRB400 steel reinforcement. Fig. 3 illustrates the uniaxial tensile stress-strain curves of the Fe-SMA rebars before and after 6 % pre-straining, along with their characteristic values. Fe-SMA is an alloy without a distinct yield plateau, so its yield strength is represented by the stress corresponding to 0.2 % plastic strain (Proof stress of 0.2 %, $R_{\rm P0.2}$).

Table 2 presents the recovery stress of Fe-SMA rebars under different pre-strain levels and activation temperatures [43,46]. Considering the potential damage to the Fe-SMA and mortar interface caused by excessively high temperatures [49], and the adverse effect of higher pre-strain on the ductility of Fe-SMA, a pre-strain of 6 % and an activation temperature of 200 °C were selected for this

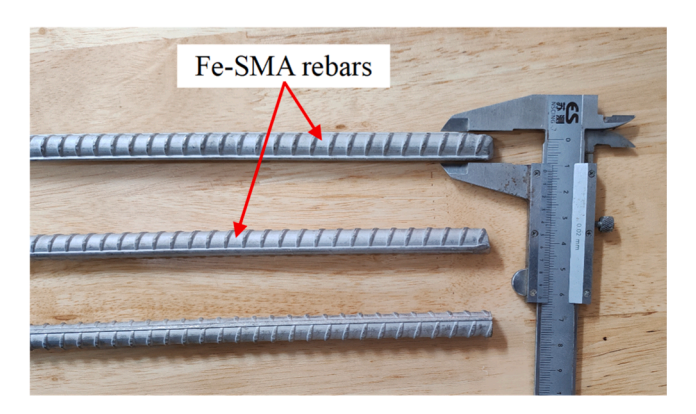


Fig. 2. Pickled Fe-SMA rebars.

Table 1Parameters of Fe-SMA rebars and steel bars.

| Reinforcement type | Diameter (mm) | Elasticity modulus (GPa) | Proof strength of 0.2 %/ $\sigma_{0.2}$ (MPa) | Ultimate strength (MPa) |
|------------------------|---------------|--------------------------|---|-------------------------|
| 6 % prestrained Fe-SMA | 10 | 165 | 550 | 890 |
| Non-prestrained Fe-SMA | 10 | 180 | 597 | 887 |
| HRB400 | 8 | 203 | 400 | 570 |

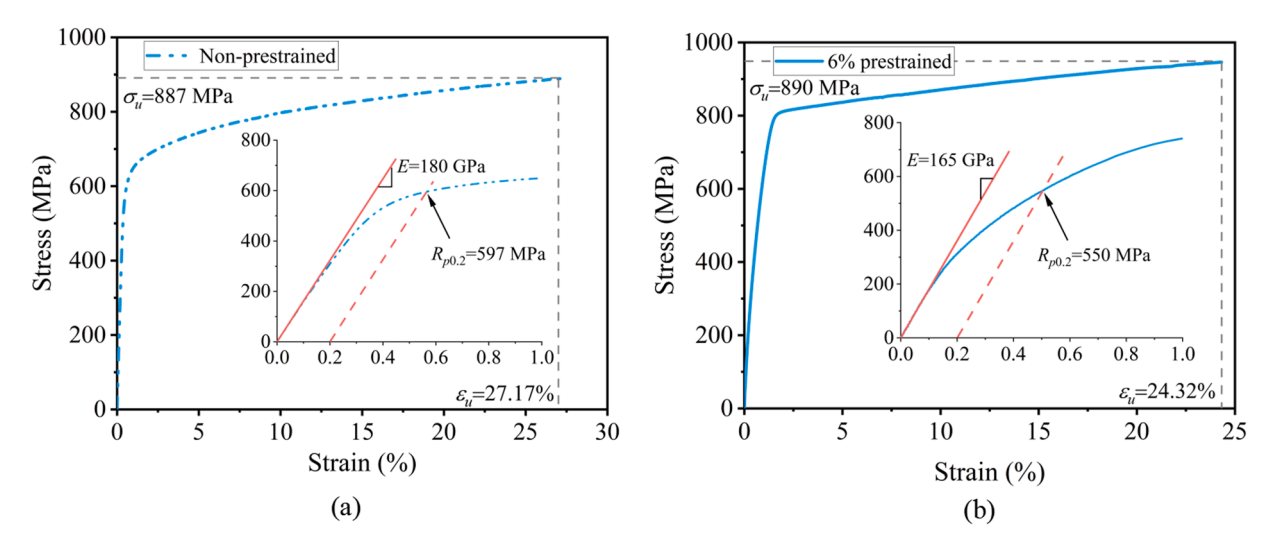


Fig. 3. Stress vs. strain curves of the Fe-SMA rebars: (a) Non-prestrained; (b) 6 % prestrained.

study [50,51,55]. The Fe-SMA rebars are employed to replace ordinary steel bars to improve crack resistance through their self-prestressing capability under high temperatures. However, the cost of Fe-SMA must be evaluated in practical engineering applications. Currently, specific cost data for domestic Fe-SMA are not publicly available. Although no official pricing information has been released, its cost is anticipated to be marginally higher than that of stainless steel bars.

2.2. Ultra-high performance concrete

The mix proportions of UHPC used in this study are presented in Table 3, with a water-to-binder ratio of 0.18 and a steel fiber volume fraction of 1.5 %. The cement used complies with the Chinese standard GB175–2007 [70], with a density of 3140 kg/m³. The average particle size of the silica fume is 0.1–0.15 μ m, and the specific surface area is between 15,000 and 27,000 m²/kg. The density of the slag powder is 2930 kg/m³, with a specific surface area of approximately 628 m²/kg. The maximum particle size of sand is 2.36 mm, which is used as fine aggregate. The superplasticizer employed has a water-reducing efficiency of over 30 %. Short straight steel fibers with a diameter of 0.2 mm and a length of 13 mm are incorporated into this UHPC mixture, exhibiting a tensile strength of 3000 MPa.

The UHPC was prepared in the laboratory, and the main production process consisted of three steps: (i) mixing and stirring the dry aggregates (cement, silica fume, slag powder, and sand) for 3 minutes to achieve a uniform blend; (ii) slowly add water and superplasticizer, and stir continuously for 8 minutes; (iii) gradually add steel fibers and stir for another 4 minutes until the UHPC reached a satisfactory level of fluidity. As specified in Chinese National Standard GB/T 50081–2019 [71], compressive strength values obtained from non-standard 100 cubic specimens require adjustment using a size correction factor. All measured strengths in this study have been multiplied by the specified factor of 0.95. The average compressive strengths of UHPC after 7, 28, and 42 days of natural curing were 60.89 MPa, 107.90 MPa, and 121.03 MPa, respectively. After 3 h of autoclave curing, the average compressive strength reached

Table 2Recovery stress of the Fe-SMA rebars under different activation temperatures.

| Prestrained level | Activated temperature (°C) | Recovery stress (MPa) | | |
|-------------------|----------------------------|-----------------------|--|--|
| 4 % | 300 | 345 | | |
| 6 % | 100 | 173 | | |
| | 200 | 331 | | |
| | 300 | 385 | | |
| 8 % | 300 | 388 | | |

Table 3 Mix proportions of UHPC and ordinary concrete (kg/m^3).

| Type of concrete | Cement | Silica fume | Slag | Coarse aggregate | Sand | Water | Superplasticizer | Steel fiber | Total weight |
|------------------|--------|-------------|------|------------------|--------|-------|------------------|-------------|--------------|
| UHPC | 705 | 217 | 163 | - | 1084.9 | 195.3 | 21.7 | 117 | 2503.9 |
| OC | 359 | 110 | 83 | 1126 | 529 | 248 | 1.7 | - | 2456.7 |

147.60 MPa. In accordance with relevant studies and conventional concrete research, the conversion factor between the cylindrical compressive strength ($f_{co,U}$) and the cubic compressive strength ($f_{cu,U}$) of UHPC is defined as 0.8 [72]. Since the experiments were conducted following 42 days of natural curing, the converted cylindrical compressive strength of UHPC ($f^*_{co,U}$) after natural curing and after autoclave curing was calculated as 96.82 MPa and 118.08 MPa, respectively.

2.3. Ordinary concrete

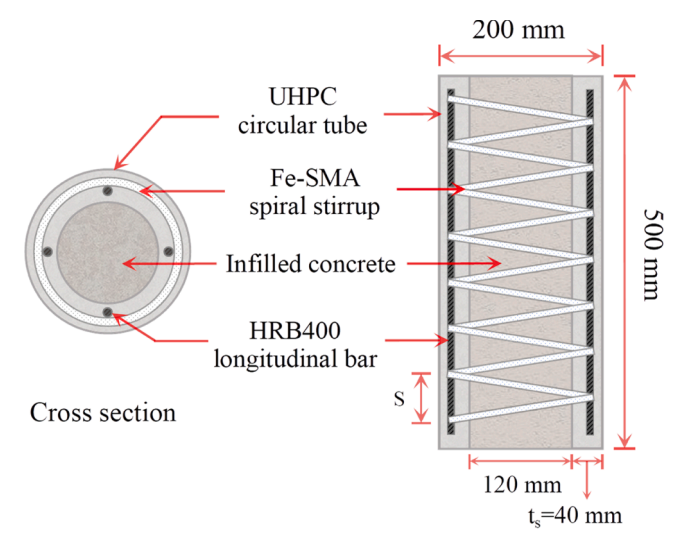
The mix proportion of the ordinary concrete is shown in Table 3 below. The compressive strength of the cast concrete is C50, and the materials used are consistent with those for UHPC, except for the coarse aggregate, which consisted of gravel with a particle size of 4.75–12.5 mm. The binder used was P.I. 42.5 Portland cement. Six 100 mm cubic specimens were cast for compressive strength testing [71]. The average compressive strengths of ordinary concrete at 7 days and 28 days were 32.94 MPa and 45.01 MPa, respectively. Following 3 h of autoclave curing, the average compressive strength was measured as 51.30 MPa. Similarly, the conversion factor between the cylindrical compressive strength of ordinary concrete ($f_{co,O}$) and the cubic compressive strength of ordinary concrete ($f_{co,O}$) is 0.8 [72]. In this study, the compressive strength of the cast-in-place ordinary concrete column after natural curing and after autoclave curing was calculated as 36.01 MPa and 41.04 MPa, respectively.

3. Experiment program

3.1. Specimens details

In this study, a total of 24 Fe-SMA spiral stirrup-reinforced Concrete-filled UHPC tubes (CFUT) were prepared, and the effects of whether Fe-SMA was pre-strained, curing methods, Fe-SMA stirrup spacing, and different concrete types on their compression performance were investigated. The longitudinal and cross-sectional views of the specimens are shown in Fig. 4, where "S" denotes the spiral stirrup spacing. Detailed specifications of the specimens are provided in Table 4. Each specimen has a diameter of 200 mm and a height of 500 mm.

To facilitate identification, the specimens are named based on different test variables. The specimen names follow a structured format: (1) The first letter donates the outer tube material ("U" for UHPC, "O" for ordinary concrete); (2) The second letter indicates internal concrete presence ("O" for ordinary concrete, "N" for none); (3) The third letter represents curing method ("N" for natural curing, omitted for autoclave curing). The second part indicates the pre-strain level of the Fe-SMA spiral stirrups, with "F6" representing a pre-strain level of 6 %, "F0" indicating no pre-strain, and "N" denoting the absence of the Fe-SMA spiral stirrups. The third



Longitudinal section

Fig. 4. Longitudinal and cross-sectional views of concrete-filled Fe-SMA spiral stirrup-reinforced UHPC tubular column.

Case Studies in Construction Materials 22 (2025) e04879

Table 4 Specific details of the specimens.

| Specimen | Type of outer tube concrete | Whether infilled concrete | Stirrup type | Fe-SMA pre-strain level (%) | Curing condition | Stirrup spacing (S) (mm) | Number of specimens |
|-----------|-----------------------------|---------------------------|--------------|-----------------------------|------------------|--------------------------|---------------------|
| UO-F6-60 | UHPC | Y | Fe-SMA | 6 | Autoclave curing | 60 | 3 |
| UO-F0-60 | UHPC | Y | Fe-SMA | 0 | Autoclave curing | 60 | 3 |
| UON-F6-60 | UHPC | Y | Fe-SMA | 6 | Natural curing | 60 | 3 |
| UON-F0-60 | UHPC | Y | Fe-SMA | 0 | Natural curing | 60 | 3 |
| OO-F6-60 | OC | Y | Fe-SMA | 6 | Autoclave curing | 60 | 2 |
| OO-F0-60 | OC | Y | Fe-SMA | 0 | Autoclave curing | 60 | 2 |
| UN-F6-60 | UHPC | N | Fe-SMA | 6 | Autoclave curing | 60 | 1 |
| UN-F0-60 | UHPC | N | Fe-SMA | 0 | Autoclave curing | 60 | 1 |
| UO-F6-80 | UHPC | Y | Fe-SMA | 6 | Autoclave curing | 80 | 1 |
| UO-F6-100 | UHPC | Y | Fe-SMA | 6 | Autoclave curing | 100 | 1 |
| UO-N | UHPC | Y | - | - | Autoclave curing | - | 1 |
| UN-N | UHPC | N | - | - | Autoclave curing | - | 1 |
| UON-N | UHPC | Y | - | - | Natural curing | - | 1 |
| UNN-N | UHPC | N | - | - | Natural curing | - | 1 |

Notes: "U"-UHPC; "O/OC"-Ordinary Concrete; "F6"-The pre-strain level of Fe-SMA is 6 %; "F0"-The pre-strain level of Fe-SMA is 0 %; "Y"-Yes; "N"-No

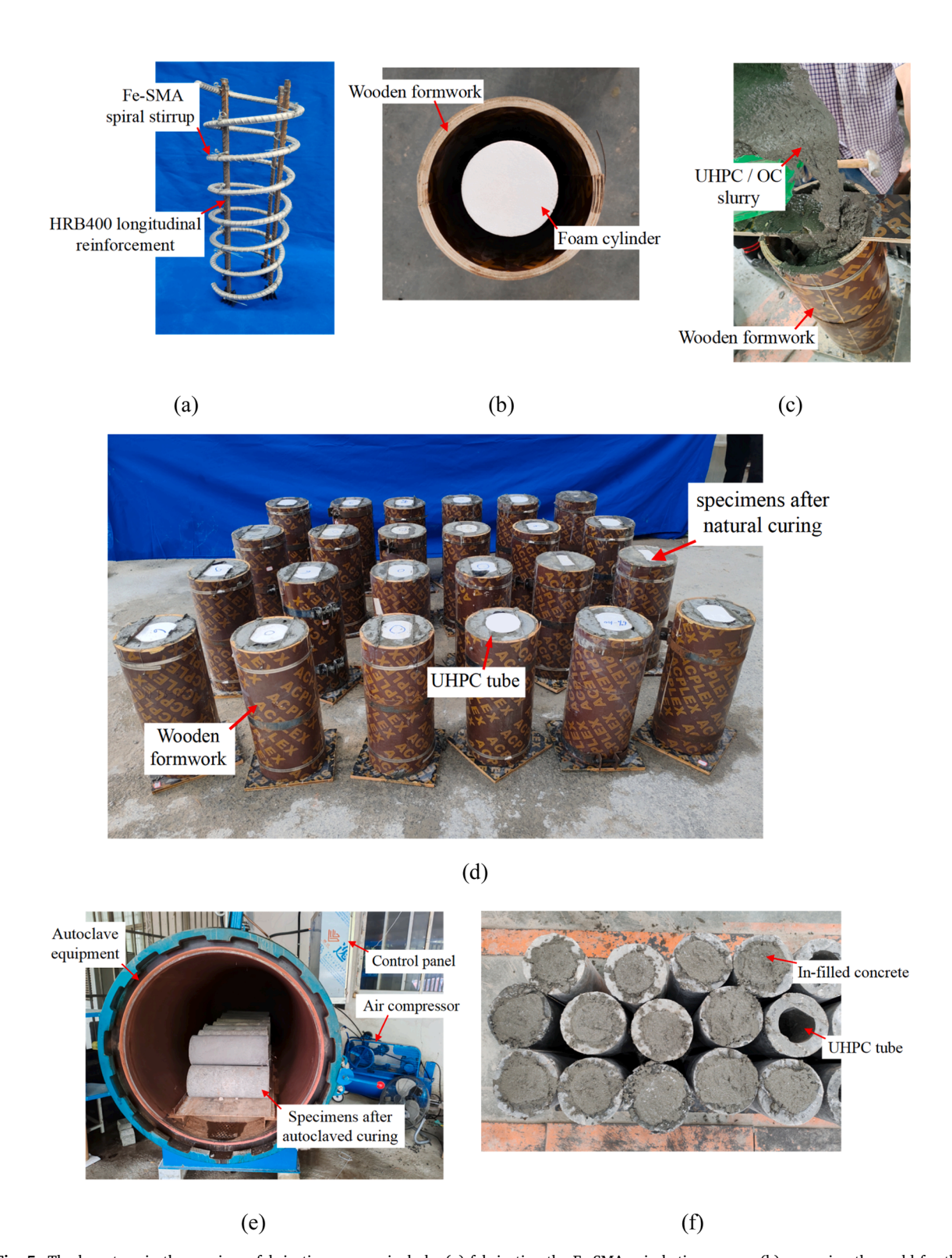


Fig. 5. The key steps in the specimen fabrication process include: (a) fabricating the Fe-SMA spiral stirrup cage; (b) preparing the mold for the UHPC tube; (c) casting the UHPC/ordinary concrete slurry; (d) natural curing of the Fe-SMA-reinforced UHPC tube for 6 days; (e) transferring to the autoclave for curing; (f) casting ordinary concrete slurry in the middle section of the UHPC tube.

part specifies the spacing of the Fe-SMA stirrups, such as "60" for a spacing of 60 mm and "80" for a spacing of 80 mm. For example, "UO-F6-60" represents a specimen with a UHPC outer tube, cast-in-place ordinary concrete core, Fe-SMA spiral stirrup with a prestrain level of 6 % embedded in the UHPC tube, a stirrup spacing of 60 mm, and autoclave curing.

3.2. Specimens preparations

The fabrication process of concrete-filled self-prestressed Fe-SMA spiral stirrups reinforced UHPC tubular columns involved the following key steps: (1) Forming Fe-SMA rebars into spiral stirrups and binding them with four HRB400 reinforcement bars to create a spiral stirrup cage. According to Ji et al. [61], the fabrication process has a negligible effect on the shape memory effect of the Fe-SMA. (2) Preparing the mold for the UHPC tube and position the Fe-SMA spiral stirrup cage, followed by casting the prepared UHPC or ordinary concrete slurry. The core mold used for casting the UHPC tube was an expanded polystyrene (EPS) foam cylinder, and the intentionally roughened inner surface of the cast UHPC tube enhances the bonding effect with the internal concrete. (3) Subjecting the Fe-SMA-reinforced UHPC tubes to natural curing for 6 days under ambient conditions (20–25 °C, \geq 60 % relative humidity). (4) Demolding the specimens and performing autoclave curing; (5) Removing the autoclave-cured Fe-SMA-reinforced UHPC tubes and casting prepared ordinary concrete in the middle section of the tube; (6) Curing the specimens under natural conditions for 28 days to complete the fabrication. To prevent localized failure at the specimen ends during axial compression, CFRP strips with a width of 6 cm were wrapped around the ends for 5 cycles. Additionally, the ends of each specimen were ground flat to ensure uniform pressure application during axial compression. Fig. 5 illustrates the key preparation process of the specimens.

After 6 days of natural curing, the Fe-SMA-reinforced UHPC tubes were demolded and subjected to autoclave curing at a temperature of 200 °C and a pressure of 1.6 MPa for 3 h. After the curing process, no obvious cracking is observed on the surface of the specimens. The high-temperature and high-pressure environment within the autoclave not only promotes the hydration reaction of the cementitious paste in UHPC [64,65], reducing harmful internal pores and enhancing density, thereby improving the overall mechanical properties of UHPC [66,67]; but also activates the shape memory effect of Fe-SMA [61], thus applying circumferential prestress to the UHPC tube after autoclave curing and cooling [68], achieving a synergistic outcome [73].

3.3. Test instrumentations and procedures

The axial compression tests were conducted on a compression testing machine with a maximum capacity of 5000 kN, and the displacement loading rate was controlled at 0.2 mm/min. The Fig. 6(a) provides a detailed view of the compression process, while Fig. 6(c) presents a top view of the specimen during testing, illustrating the specific locations of the linear variable displacement transducers (LVDTs) and strain gauges (SGs). Previous studies have demonstrated that high-strength gypsum is essential for ensuring uniform pressure distribution during compression [74]. Therefore, high-strength gypsum was applied to the upper and lower end surfaces of the specimens, and loading commenced after the gypsum had cooled and hardened.

In this study, LVDT1–4 were uniformly distributed at the bottom of the specimen to measure the overall loading displacement. LVDT5 and LVDT6 were positioned on the left and right sides of the upper part of the specimen, respectively, to measure the deflection of the crossbeam. The specific arrangement of the LVDTs and strain gauges is shown in Fig. 6(c). Among them, SG3, SG5, and SG7 are hoop strain gauges, placed at 10 cm from the top, the middle, and 10 cm from the bottom of the specimen, respectively. Similarly, SG4, SG6, and SG8 were positioned on the opposite side. SG1 and SG2 are axial strain gauges, symmetrically arranged in the middle section of the specimen.

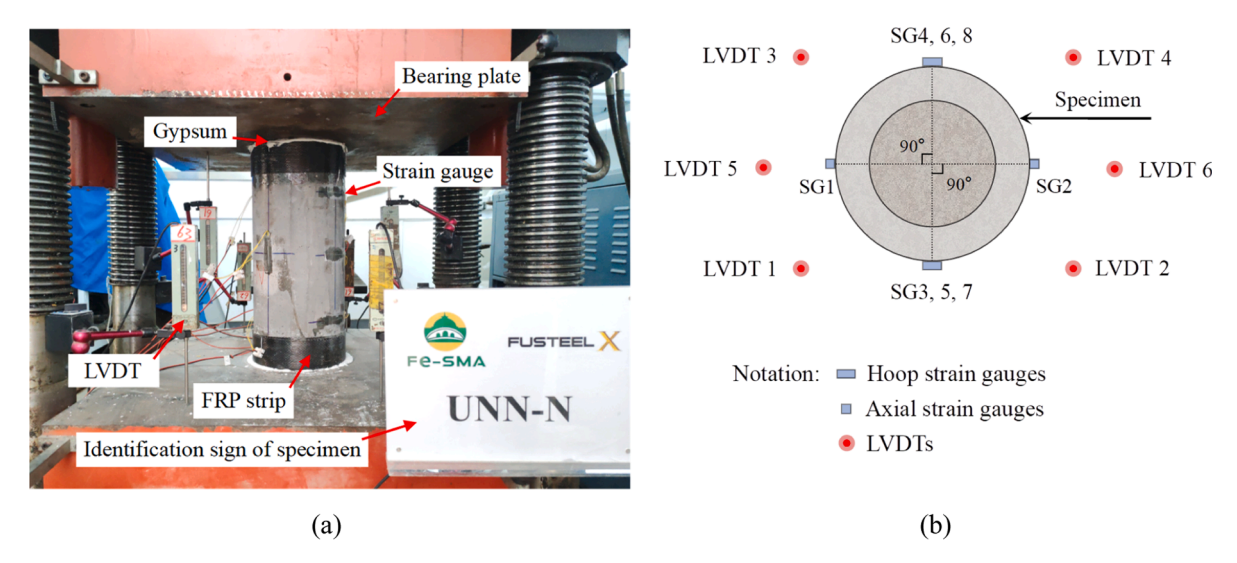
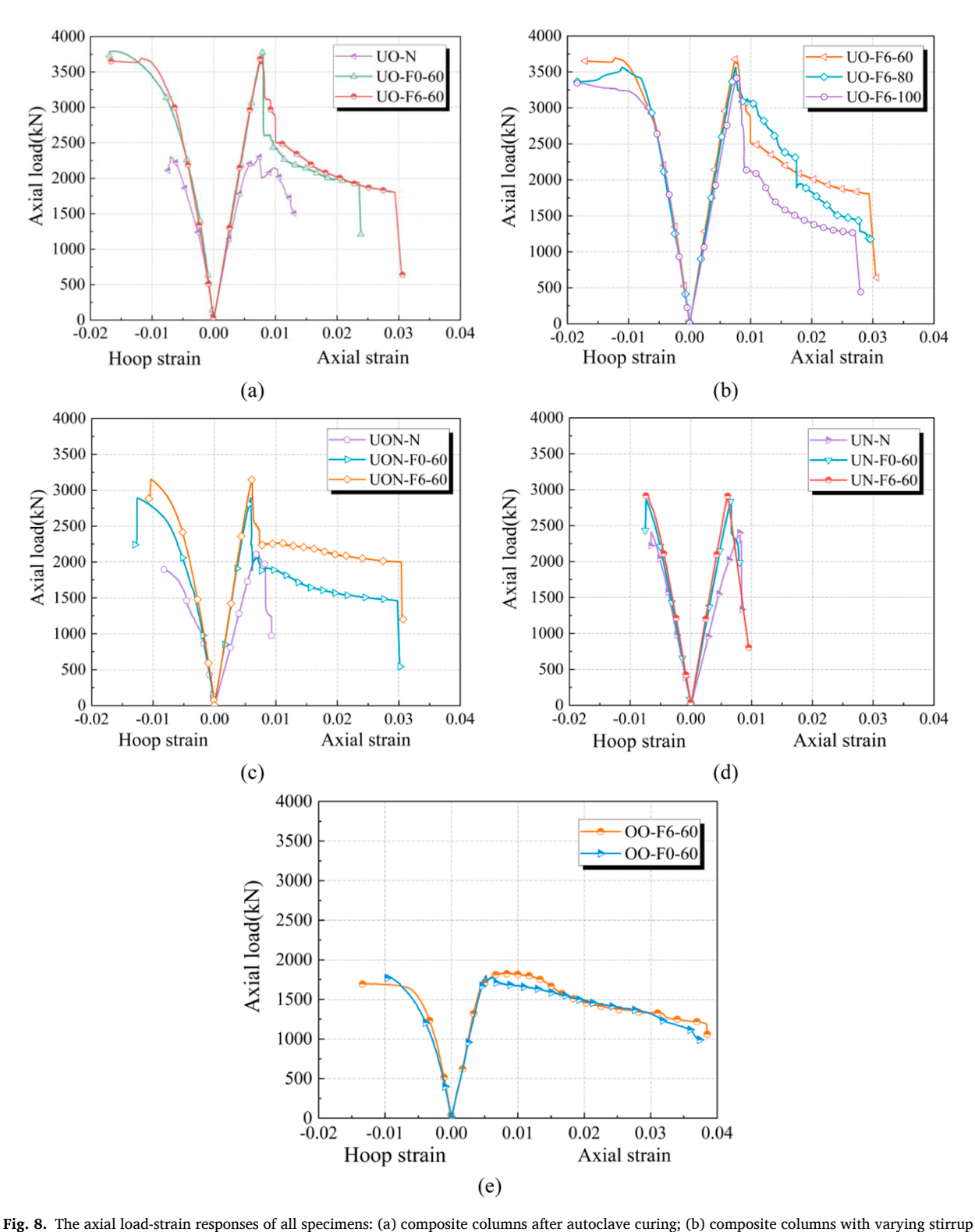


Fig. 6. The setup of axial compression test: (a) detailed view of the experiment; (b) layout of the LVDTs and strain gauges.



Fig. 7. Failure modes of specimens: (a) composite columns after autoclave curing; (b) composite columns after natural curing; (c) composite columns with varying stirrup spacing; (d) UHPC tubes after autoclave curing; (e) ordinary concrete columns and UHPC tube after natural curing.

During the axial compression test, the load data were obtained through the compression machine, while the data from the LVDTs and strain gauges were collected using the data acquisition system DH-3816. The data collection frequency of the compression machine was set at 5 Hz, and the acquisition frequency of the DH-3816 was set at 1 Hz.



spacing; (c) composite columns after natural curing; (d) UHPC tubes after autoclave curing; (e) ordinary concrete columns after autoclave curing.

4. Test results and discussion

4.1. Failure modes

As shown in Fig. 7, the specimens were categorized based on their material composition and curing methods. For composite columns reinforced with Fe-SMA spiral stirrups (UO-F6-60, UO-F0-60, UON-F6-60, and UON-F0-60), the initial loading stage was elastic, during which no visible cracks were observed on the specimen surface. Subsequently, fine cracks first appeared at the specimen ends and gradually propagated toward the middle. As loading increased, several circumferential cracks formed in the middle section of the specimen, accompanied by lateral expansion and cracking sounds. With further crack propagation, the concrete cover gradually lost its load-bearing capacity, and the axial load was primarily borne by the core area confined by Fe-SMA spiral stirrups, during which energy continuously accumulated within the composite column. When the axial displacement reached a certain level, the composite column experienced sudden brittle failure, characterized by a sharp drop in load-bearing capacity and a loud explosive sound.

For the composite columns without Fe-SMA stirrups (UO-N, UON-N), the failure mode during the initial loading stage was similar to that previously described. In the later stages of the elastic phase, several fine microcracks appeared at the ends, which gradually propagated downward and converged in the middle section of the specimen, causing lateral expansion. Unlike Fe-SMA-reinforced specimens, these columns did not exhibit a ductility stage. Instead, cracks propagated continuously until the specimens underwent a sudden brittle failure.

For Fe-SMA-reinforced UHPC tubes without internal concrete infill (UN-F6-60, UN-F0-60, UN-N, and UNN-N), as shown in Fig. 7 (d), a brittle failure mode is observed under axial loading. In the late phase of the elastic stage, several fine cracks initiate at the ends of the specimen. Subsequently, these cracks rapidly propagate either circumferentially or axially. When the circumferential cracks connect end-to-end or the axial cracks converge at the mid-section of the specimen, lateral expansion accelerates sharply, followed by a sudden drop in load-bearing capacity, leading to the ultimate failure of the specimen.

For Fe-SMA-reinforced ordinary concrete columns (OO-F6–60, OO-F0–60), as shown in Fig. 7(e), the fragmentation of the cover layer was more severe. In the mid-to-late stage of the elastic phase, several fine microcracks were observed in the middle section of the specimen. These cracks rapidly propagated, with their widths continuously increasing, leading to the formation of multiple vertical diagonal cracks. As loading progressed, the edge concrete gradually spalled, and numerous concrete fragments could be observed in the bottom of the specimen. Subsequently, large-scale spalling of the edge concrete layer occurred, and the load was primarily transferred to the core area of the composite column. The specimen then entered a prolonged ductility stage.

4.2. Load-strain behavior

As shown in Fig. 8, the load-strain curves of the specimens are categorized into five groups based on curing methods and material types. Stress-strain curves were not used because the edge concrete cracked and lost its load-bearing capacity during axial compression, leading to stress redistribution due to changes in the compression cross-section. Therefore, load-strain curves were selected for analysis. All load-strain responses include axial strain and hoop strain responses, with positive values representing axial strain on the right and negative values representing hoop strain on the left. According to previous researches [75,76], the axial strain of the specimens is represented by the total axial strain measured by LVDTs rather than the local axial strain measured by strain gauges. Following Section 3.3, the overall axial displacement is calculated by subtracting the average displacement of the two upper LVDTs from that of the four lower LVDTs. The total axial strain is calculated by dividing the overall axial displacement by the specimen height

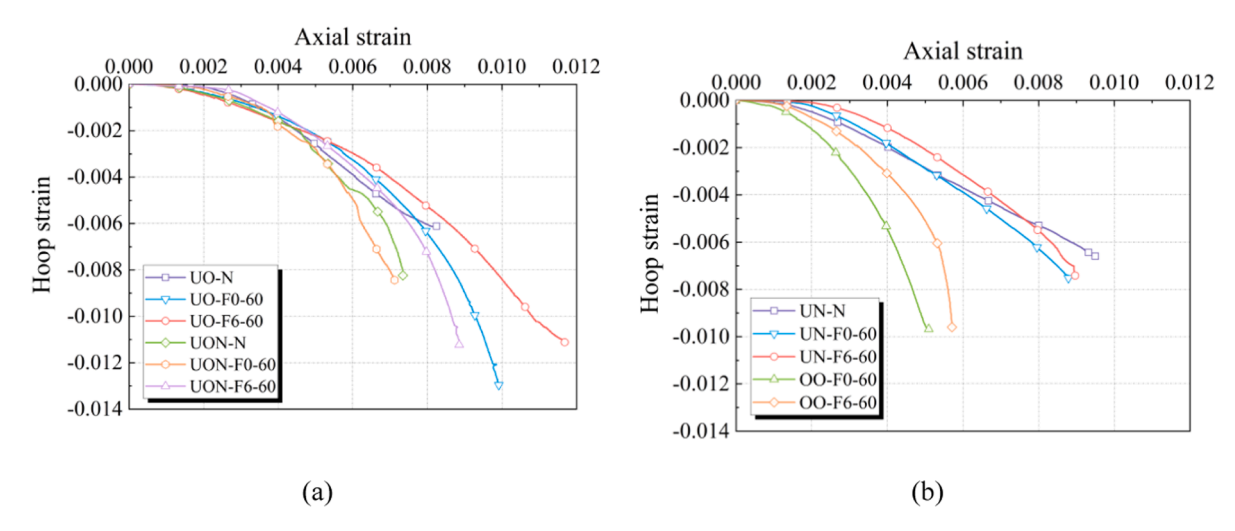


Fig. 9. The hoop strain-axial strain responses of the specimens: (a) composite columns after autoclave curing and natural curing; (b) OC columns and UHPC tubes after autoclave curing.

(500 mm), while the hoop strain is obtained from the average of six hoop strain gauges. The later stages of the hoop strain response are not shown on the opposite side of Fig. 8 due to damage to the hoop strain gauges caused by spalling of the edge concrete. The hoop strain-axial strain curves measured by strain gauges during the initial loading stage are shown in Fig. 9, reflecting the local lateral deformation of the specimens during the linear ascending phase.

In this paper, taking UO-F6–60 as an example, the load-strain response of the specimen can be observed to primarily consist of four distinct phases:

- (1) **Linear elastic ascending phase.** According to existing research [76], UHPC exhibits elastic behavior up to 90–95 % of its compressive strength, with minimal softening. During this phase, the Fe-SMA-reinforced UHPC tube effectively provides confinement to the core ordinary concrete column.
- (2) **Sudden load drop after the initial peak.** Following the elastic phase, cracks on the specimen surface rapidly propagate, leading to a sharp decline in axial load [77,78]. However, due to the active confinement provided by the Fe-SMA, the axial load exhibits a stepped-down trend instead of a sudden drop. This is because the active confinement enhances the synergy between the concrete and the stirrups, improves material utilization, and prevents brittle failure and abrupt load loss [38,39].
- (3) **Strain softening phase.** After the axial load drops to a new plateau, the edge concrete has fully cracked and ceased to function. The load is then borne by the core area of the composite column confined by Fe-SMA spiral stirrups. Subsequently, cracks continue to propagate, and lateral expansion progresses, leading to a prolonged strain softening phase.
- (4) **Brittle failure.** As the axial loading displacement increases, energy accumulates within the composite column, and cracks propagate both circumferentially and diagonally. When the internal energy reaches a critical level, the Fe-SMA spirals fracture, resulting in sudden brittle failure [78,79]. The axial load drops abruptly, accompanied by a loud explosive sound.

4.2.1. The effect of pre-straining

Compared to specimens with non-prestrained Fe-SMA, the specimens reinforced with prestrained Fe-SMA exhibited improved ultimate compressive deformation capacity and circumferential stiffness. As shown in Fig. 8(a), the ultimate compressive deformation capacity and circumferential stiffness of the prestrained specimens increased by 28.15 % and 15.77 %, respectively. The circumferential stiffness of the specimens was determined via linear regression analysis of the stress-strain curve within the 20 %–70 % range of the ultimate compressive strength. This improvement can be attributed to the active circumferential confinement provided by the prestrained Fe-SMA spiral stirrups, which was applied to the specimens before loading to achieve synergy between the stirrups and the concrete columns, thereby preventing stress hysteresis [38,39]. Additionally, as shown in Fig. 8 and Fig. 9, active confinement reduced the initial damage to UHPC tubes, improved the material utilization, and fully utilized the strength of the UHPC and inner concrete core [40,41].

Compared to composite columns reinforced with Fe-SMA, the active confinement provided by Fe-SMA had a more pronounced effect on enhancing the load-bearing capacity and stiffness of UHPC tubes or OC columns. As shown in Fig. 8(a) and Fig. 9, whether Fe-SMA was prestrained had minimal impact on the ultimate load-bearing capacity and stiffness of CFUT. For UHPC tubes and OC columns, the active confinement of Fe-SMA spiral stirrups slightly improved the ultimate load-bearing capacity, while the elastic stiffness increased by 12.14 % and 6.37 %, respectively, as shown in Fig. 8(d) and (e). This was primarily because the lower the concrete strength or structural stiffness, the greater the contribution of the active confinement of Fe-SMA to the load-bearing performance, resulting in more significant improvements.

The active confinement provided by Fe-SMA effectively mitigated the brittle failure of specimens. As shown in Fig. 8(a), during the post-peak load descending stage, the axial load of the prestrained specimen (UO-F6–60) decreased more gradually compared to the abrupt drop observed in the non-prestrained specimen (UO-F0–60). The load reduction exhibited a stepwise trend, and the load values during the strain softening phase were higher than those of the non-prestrained specimens.

4.2.2. The effect of different curing methods

Compared to natural curing, the specimens subjected to autoclave curing exhibited higher ultimate load-bearing capacity. For instance, CFUT columns reinforced with 6 % and 0 % prestrained Fe-SMA spirals showed increases in ultimate load-bearing capacity of 17.03 % and 31.20 %, respectively. This improvement is attributed to the accelerated hydration reaction within the UHPC tube during autoclave curing, which increased compressive strength of UHPC.

Unlike autoclave-cured specimens, the ultimate compressive deformation capacity of specimens after natural curing showed little difference. However, both the ultimate load-bearing capacity and load values during the strain-softening stage were higher for the specimens reinforced with 6 % prestrained Fe-SMA. For composite columns without stirrup confinement, both the stiffness and compressive deformation capacity of the specimens improved after autoclave curing. Compared to natural curing, the stiffness of the autoclave-cured specimens increased by 29.73 %, and the ultimate compressive deformation capacity improved by 40.41 %. Additionally, unlike the sharp load drop observed in the post-elastic phase of naturally cured specimens, the load decrease in autoclave-cured specimens was more gradual. This indicates that autoclave curing plays a significant role in mitigating brittle failure and enhancing the ductility of composite columns.

4.2.3. The effect of different Fe-SMA stirrup spacing distances

As the spacing of the Fe-SMA stirrups decreased, both the stiffness in the elastic phase and the load values during the strain softening phase of the specimens improved to varying degrees. Taking the lowest point of the strain softening phase of the specimen

UO-F6–100 as a reference, the load values of UO-F6–80 and UO-F6–60 increased by 13.66 % and 38.95 %, respectively, while the stiffness in the elastic phase improved by 5.61 % and 11.54 %. The load during the strain-softening phase is primarily borne by the core area of the composite column confined by Fe-SMA stirrups. As the spacing of the stirrups decreases, the confinement effect of Fe-SMA becomes more effective, resulting in higher strength of the core confined concrete.

Decreasing Fe-SMA stirrup spacing within an optimal range helps mitigate brittle failure and enhances specimen ductility. As shown in Fig. 8(b), for specimen UO-F6–100, the specimen experienced a sharp load drop after the peak load in the elastic stage, followed by a prolonged strain-softening phase upon reaching a new load plateau. On the other hand, for specimens UO-F6–60 and UO-F6–80, the load exhibited a stepwise decline after the peak in the elastic stage, eventually reaching a new load plateau and undergoing strain-softening. This indicates that a certain degree of smaller Fe-SMA spiral spacing is beneficial to prevent a sudden decline in the load-bearing capacity of the specimens and avoiding brittle failure.

4.2.4. The effect of different concrete types

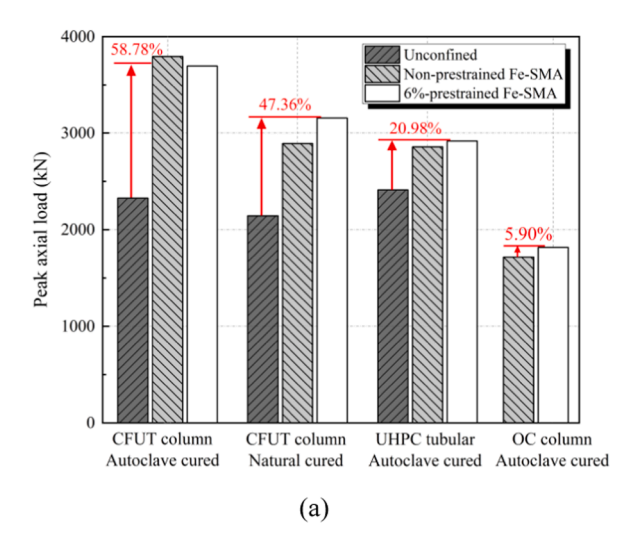
As shown in Fig. 8(e), unlike specimens with UHPC outer tubes, those with OC outer tubes do not exhibit significant sudden brittle failure during compression. Instead, they undergo a prolonged strain-softening stage after reaching the peak load. This phenomenon is consistent with the findings of Yeon et al. [80]. For OC columns, the ultimate axial strain is defined as the strain at 75 % of the ultimate load [81]. The ultimate axial strains for OO-F0–60 and OO-F6–60 are 0.0223 and 0.02549, respectively, indicating that the active confinement provided by Fe-SMA enhances the ultimate axial strain of OC columns by 14.31 %.

Compared to specimens with UHPC outer tubes, the active confinement provided by Fe-SMA demonstrates a more significant enhancement in the ultimate load-bearing capacity and circumferential stiffness of specimens with OC outer tubes, as shown in Fig. 8 (a) and (e). This is because the compressive strength of UHPC is much higher than that of OC (approximately 3–4 times greater), and the prestress generated by Fe-SMA contributes more to OC columns. As a result, the improvements are more pronounced for OC columns.

4.3. Peak load and strain

The peak axial loads and ultimate axial strains of key specimens are shown in Fig. 10, with the main results summarized in Table 5. Under the active confinement of Fe-SMA, both the peak loads and ultimate strains of the specimens exhibit varying degrees of improvement. For CFUT columns reinforced with Fe-SMA stirrups, there is a significant increase in both the peak axial load and ultimate strain, and similar improvements are observed for UHPC tubes reinforced with Fe-SMA. For example, the peak load and ultimate strain of unconfined CFUT columns after autoclave curing are 2327.04 kN and 0.01305, respectively, while those of the CFUT columns reinforced with 6 % prestrained Fe-SMA stirrups are 3694.75 kN and 0.03060, representing increases of 58.78 % and 26.35 %, respectively. For UHPC tubes reinforced with Fe-SMA stirrups, the peak load and ultimate axial strain increase by 20.98 % and 26.35 %, respectively. This indicates that the active confinement of Fe-SMA contributes more significantly to the axial compression performance of CFUT compared to UHPC tubes.

Compared to natural curing, CFUT columns reinforced with Fe-SMA stirrups exhibit higher peak loads after autoclave curing. For instance, the peak loads of CFUT columns reinforced with 0 % and 6 % prestrained Fe-SMA stirrups after natural curing are 2891.52 kN and 3157.21 kN, while after autoclave curing, they increase to 3793.63 kN and 3694.75 kN, representing improvements of 31.20 % and 17.03 %, respectively. For OC columns, the active confinement of Fe-SMA also improves the peak load and ultimate strain to some extent, with increases of 5.90 % and 14.31 %, respectively. Therefore, the active confinement of Fe-SMA improves the peak load and ultimate strain of CFUT columns, UHPC tubes, and OC columns. Autoclave curing is beneficial for enhancing the



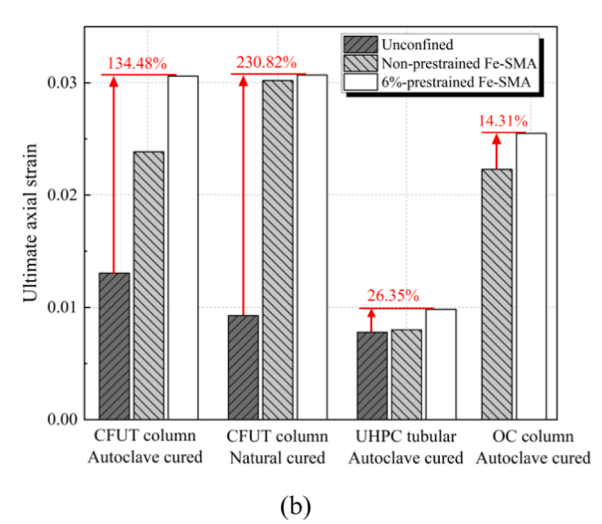


Fig. 10. Peak axial loads and ultimate axial strains of the specimens: (a) peak axial loads; (b) ultimate axial strains.

Table 5Summary of the key results for specimens.

| Specimen | $F_{c\iota\nu}$ F_{cc} (kN) | F_{cc} / F_{cu} | $arepsilon_{	extit{cw}} \; arepsilon_{	extit{cc}}$ | $arepsilon_{cc}$ / $arepsilon_{cu}$ |
|-----------|-------------------------------|-------------------|--|-------------------------------------|
| UO-N | 2327.04 | 1 | 0.01305 | 1 |
| UO-F0-60 | 3793.63 | 1.63 | 0.02386 | 1.83 |
| UO-F6-60 | 3694.75 | 1.59 | 0.03060 | 2.34 |
| UON-N | 2142.56 | 1 | 0.00928 | 1 |
| UON-F0-60 | 2891.52 | 1.35 | 0.03021 | 3.26 |
| UON-F6-60 | 3157.21 | 1.47 | 0.03070 | 3.31 |
| UN-N | 2412.01 | 1 | 0.00778 | 1 |
| UN-F0-60 | 2857.67 | 1.18 | 0.00800 | 1.03 |
| UN-F6-60 | 2917.97 | 1.21 | 0.00983 | 1.26 |
| OO-F0-60 | 1729.04 | 1 | 0.02230 | 1 |
| OO-F6-60 | 1816.86 | 1.05 | 0.02549 | 1.14 |

ultimate load-bearing capacity of specimens. The CFUT columns reinforced with self-prestressed Fe-SMA spiral stirrups proposed in this study demonstrates significant potential in improving the ultimate load-bearing capacity of specimens and mitigating brittle failure.

5. Verifying calculation for predicting the ultimate axial load of specimens

5.1. Calculation of section bearing capacity of concrete-filled Fe-SMA-reinforced UHPC tubular column

When calculating the compressive load-bearing capacity of the Fe-SMA spiral stirrup-reinforced CFUT section, the model proposed and validated by Mander et al. [82] for stirrup-confined concrete is adopted. The area within the centerline of Fe-SMA stirrup is divided into the core region, consisting of confined UHPC and ordinary concrete, while the area outside the Fe-SMA stirrup is the unconfined UHPC cover. For the sectional analysis of Fe-SMA-reinforced CFUT columns, as shown in Fig. 11, the load-bearing capacity is divided into four contributing parts: the core-confined ordinary concrete, the confined UHPC, the unconfined UHPC outside the Fe-SMA stirrups, and the longitudinal bars. Therefore, the relationship between the sectional load-bearing capacity of Fe-SMA reinforced CFUT and its contributing components is expressed as Eq. (1):

$$N_u = f'_{co}A_{co} + f'_{cc,uhpc}A_{cc,uhpc} + f'_{cc,oc}A_{cc,oc} + f_bA_b$$

$$\tag{1}$$

Where N_u represents the total sectional load-bearing capacity of Fe-SMA reinforced CFUT; f ' $_{co}$, A_{co} denote the stress and area of the unconfined UHPC outside the centerline of the Fe-SMA stirrup; f ' $_{cc,uhpc}$ and $A_{cc,uhpc}$ represent the stress and area of the confined UHPC; f ' $_{cc,oc}$ and $A_{cc,oc}$ correspond to the stress and area of the core-confined ordinary concrete; and f_b and A_b indicate the axial stress and area of the longitudinal bar, respectively.

To accurately predict the stress of confined UHPC, Bing et al. [84] modified the classical Mander model [82,83] based on the experimental results of Khaloo et al. [85], and proposed an expression (Eq. (2)) for the peak stress of core-confined concrete, which is more suitable for high-strength concrete:

$$f'_{cc} = f'_{co} \left(-0.413 + 1.413 \sqrt{1 + 11.4 \frac{f_l}{f'_{co}}} - 2 \frac{f_l}{f'_{co}} \right)$$
 (2)

Here, f 'cc is the peak stress of confined concrete, f 'co is the compressive strength of unconfined concrete, and fl is the effective confinement stress from Fe-SMA spiral stirrups, computed using Eq. (3) from Mander et al. [82]

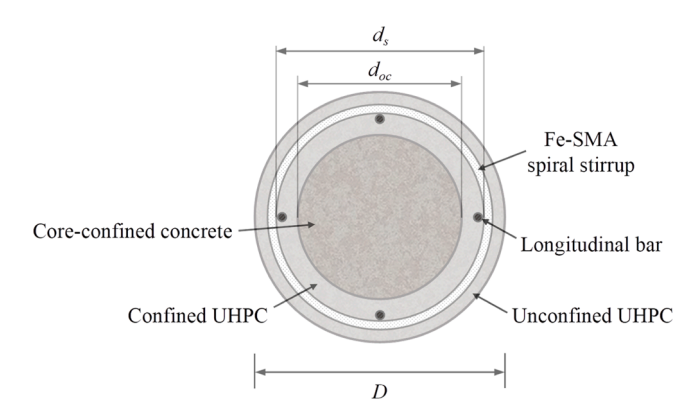


Fig. 11. Cross-sectional diagram of specimen.

$$f_l = \frac{2k_e A_F f_{F,e}}{d.s} \tag{3}$$

Where d_s represents the diameter of the core concrete confined by the Fe-SMA spiral stirrup; A_F and s denote the cross-sectional area and spacing of the Fe-SMA stirrup, respectively; $f_{F,e}$ indicates the effective stress of the Fe-SMA spiral stirrup, with the specific calculation detailed in Section 5.2; and k_e is the effective confinement coefficient calculated by Eq. (4) [82].

$$k_e = \frac{1 - \frac{s'}{2d_s}}{1 - \rho_{cc}} \tag{4}$$

Where s' is the clear spacing of the Fe-SMA spiral stirrup; and ρ_{cc} represents the ratio of the cross-sectional area of the longitudinal bar to the cross-sectional area of the core concrete.

5.2. Calculation of effective stress in Fe-SMA spiral stirrup

When calculating the effective stress $f_{F,e}$ of the Fe-SMA spiral stirrup, for unactivated Fe-SMA rebars (e.g., under natural curing or non-prestrained), $f_{F,e} = f_{F,y}$ is adopted based on the study by Mander et al. [82], where $f_{F,y}$ is the proof strength of 0.2 % of the Fe-SMA spiral stirrup. For activated Fe-SMA stirrups (i.e., prestrained and autoclave-cured), considering the active circumferential confinement provided by Fe-SMA spiral stirrups, the effective stress $f_{F,e}$ is the stress at the corresponding strain [80], which is calculated according to the following method. The theories of elasticity and small deformation are adopted in this study [85,88].

Firstly, it is necessary to determine the effective stress of the Fe-SMA spiral stirrups at the strain corresponding to the peak load. According to the research of Jian et al. [86], the relationship between the lateral strain ε_l and the axial stain ε_c of concrete columns under active confinement can be expressed by Eq. (5) as follows.

$$\varepsilon_c = \frac{\varepsilon_l}{v_l \left[1 + \left(\frac{\varepsilon_l}{v_l \varepsilon_{co}}\right)^n\right]^{1/n}} + 0.04\varepsilon_l^{0.7} \left[1 + 21\left(\frac{f_l}{f'_{co}}\right)^{0.8}\right]$$
(5)

Where v_i is the Poisson's ratio of the confined concrete column, calculated according to Eq. (6) proposed by Candappa et al. [87]; n is the shape factor of the curve; and ε_{co} is the peak strain of unconfined concrete, both calculated using Eqs. (7) and (8) proposed by Tasdemir et al. [88], respectively.

$$v_i = 8 \times 10^{-6} f_{co}^2 + 0.0002 f_{co}^2 + 0.138$$
 (6)

$$\varepsilon_{co} = (-0.067f_{co}^2 + 29.9f_{co}' + 1053) \times 10^{-6}$$
 (7)

$$n = 1 + 0.03 t_{co}$$
 (8)

In this study, to simplify the calculations, a bi-linear model is adopted to approximate the stress-strain curve of the activated Fe-SMA rebars [80]. The stress of the activated Fe-SMA rebar at any given strain can be approximately calculated using Eq. (9):

$$f_{F,e} = \begin{cases} f_{F,r} + E_F \epsilon_F & 0 \le \epsilon_F \le \epsilon_{F,y} \\ f_{F,y} + E_{F,s} (\epsilon_F - \epsilon_{F,y}) & \epsilon_{F,y} < \epsilon_F \le \epsilon_{F,u} \end{cases}$$

$$(9)$$

Where $f_{F,e}$ is the effective stress of Fe-SMA rebar at any strain; $f_{F,r}$ and $f_{F,y}$ are the recovery stress and the yield strength of the Fe-SMA

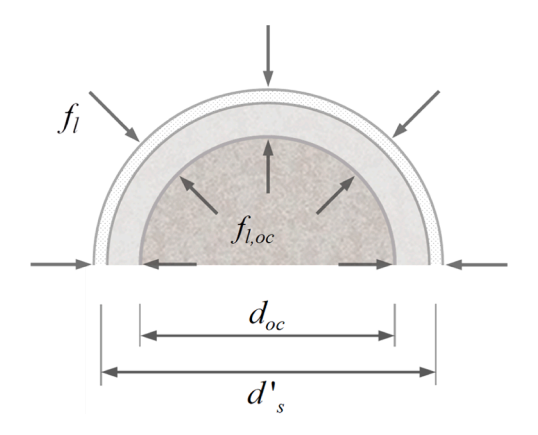


Fig. 12. Stress analysis schematic diagram of confined UHPC tube.

rebar, respectively; ε_F is the strain of the Fe-SMA rebar. In this study, it is assumed that $\varepsilon_F = \varepsilon_b$ as referenced in [80]; $\varepsilon_{F,y}$ and $\varepsilon_{F,u}$ are the yield strain and ultimate strain of Fe-SMA, respectively; E_F and $E_{F,s}$ are the elastic modulus of the Fe-SMA rebar in the elastic stage and strain-hardening stage, respectively, with $E_{F,s}$ calculated according to Eq. (10).

$$E_{F,s} = \frac{f_{F,u} - f_{F,y}}{\varepsilon_{F,u} - \varepsilon_{F,y}} \tag{10}$$

5.3. Calculation of stress in core-confined ordinary concrete

When calculating the stress of the core-confined ordinary concrete, the core-confined UHPC is subjected to stress analysis as an isolated body, as shown in Fig. 12. The relationship between the effective confinement stress acting on the ordinary concrete $f_{l,oc}$ and the effective confinement stress provided by the Fe-SMA stirrups f_l is as follows:

$$f_{l,oc} = k_t f_l = \frac{\pi d_s'}{\pi d_{or}} f_l = \frac{d_s'}{d_{or}} f_l$$
 (11)

Where k_t is the conversion coefficient, $k_t = \frac{d'_s}{d_{oc}}$; d's represents the distance between the centerlines of the Fe-SMA stirrup; and d_{oc} is the diameter of the core-confined ordinary.

After determining the effective confinement stress provided by the Fe-SMA stirrups f_b the effective confinement stress of the core-confined ordinary concrete $f_{l,oc}$ is calculated using Eq. (11). Subsequently, the compressive strength of core-confined ordinary concrete is calculated using Eq. (12) proposed by Mander et al. [82].

$$f'_{cc,oc} = f'_{co,oc} \left(-1.254 + 2.254 \sqrt{1 + 7.94 \frac{k_t f_{l,oc}}{f'_{co,oc}}} - 2 \frac{k_t f_{l,oc}}{f'_{co,oc}} \right)$$
(12)

Where $f'_{co,oc}$ represents the compressive strength of the unconfined ordinary concrete.

5.4. Verifying calculation for the load carrying capacity of specimens

In summary, the compressive strength of the confined UHPC $f'_{cc,uhpc}$, the compressive strength of the core-confined ordinary concrete $f'_{cc,oc}$, the effective confinement stress of the Fe-SMA stirrup f_l , the calculated load capacity N and the tested load capacity N_u are presented in Table 6. The comparison between the calculated and tested values is shown in Fig. 13. Additionally, the degree of deviation D shown in Table 6 is calculated according to Eq. (13).

$$D = \frac{N_u - N}{N_u} \times 100\% \tag{13}$$

As shown in Table 6 and Fig. 13, the tested and calculated values of peak load are in good agreement, indicating the effectiveness of the proposed calculation method. This method accurately predicts the axial compressive capacity of CFUT columns reinforced with Fe-SMA spiral stirrups, providing valuable insights for the design of such composite columns. Some deviations may result from natural variations in concrete strength. Further research should examine bond-slip behavior between Fe-SMA rebar and the UHPC matrix, as well as concrete creep effects on prestress loss.

6. Conclusions

This paper proposed a novel form of concrete-filled self-prestressed Fe-SMA spiral stirrup-reinforced UHPC tubular column. Autoclave curing was adopted to simultaneously achieve the objectives of enhancing the strength of UHPC and activating the Fe-SMA spirals to provide active confinement. Axial compression tests were conducted to investigate the effects of pre-straining, different curing methods, and the spacing of Fe-SMA stirrups on the compressive performance. The following conclusions can be drawn from the results and the relative discussions:

- (1) The stress-strain curves of the specimens exhibit four distinct stages: linear elasticity, sudden load drop, strain softening, and failure. Active confinement from Fe-SMA results in a more gradual load drop following the linear elastic stage.
- (2) The active confinement provided by Fe-SMA is beneficial for suppressing the lateral expansion, enhancing the compressive deformation capacity and stiffness of the specimens. Compared to passive confinement, the deformation capacity and circumferential stiffness increase by 28.15 % and 15.77 %, respectively.
- (3) The axial load during the strain-softening stage is primarily borne by the core-confined area of the composite columns. With the decrease of Fe-SMA stirrup spacing, the peak load, elastic stiffness and the load during strain-softening stage show a decreasing trend, which indicates their reducing confinement efficiency.
- (4) The failure mode of the specimens is characterized by the appearance of several micro-cracks at the ends and converge in the mid-section, causing lateral expansion and edge concrete loses its load-bearing capacity. When the internal energy accumulates to a certain level, brittle failure occurs, accompanied by the fracture of Fe-SMA stirrups.

Table 6
Comparison of the calculated and tested peak axial loads of specimens.

| Specimen | f' co or f ' cc,uhpc (MPa) | $f'_{cc,oc}$ (MPa) | f_l (MPa) | Calculated load N (kN) | Tested load N_u (kN) | Deviation (%) |
|-----------|------------------------------|--------------------|-------------|--------------------------|------------------------|---------------|
| UO-N | 118.08 | 36.01 | - | 2574.34 | 2327.04 | -9.60 |
| UO-F0-60 | 158.67 | 80.58 | 8.33 | 3545.64 | 3793.63 | 6.53 |
| UO-F6-60 | 151.93 | 74.60 | 6.70 | 3453.06 | 3694.75 | 6.54 |
| UO-F6-80 | 142.85 | 65.85 | 4.67 | 3268.37 | 3561.87 | 8.24 |
| UO-F6-100 | 137.10 | 59.83 | 3.47 | 3118.90 | 3448.74 | 9.56 |
| UON-N | 96.82 | 36.01 | - | 2191.01 | 2142.56 | -2.21 |
| UON-F0-60 | 135.88 | 80.58 | 8.33 | 3044.97 | 2891.52 | -5.04 |
| UON-F6-60 | 129.51 | 74.54 | 6.68 | 2957.61 | 3157.21 | 6.32 |
| UN-N | 118.08 | - | - | 2209.11 | 2412.01 | 8.41 |
| UN-F0-60 | 158.67 | - | 8.33 | 2725.49 | 2857.67 | 4.63 |
| UN-F6-60 | 146.00 | - | 5.35 | 2692.73 | 2917.97 | 7.71 |
| OO-F0-60 | 71.94 | 80.58 | 8.33 | 1878.89 | 1729.04 | -7.97 |
| OO-F6-60 | 64.74 | 70.34 | 5.66 | 1726.39 | 1816.86 | 5.24 |

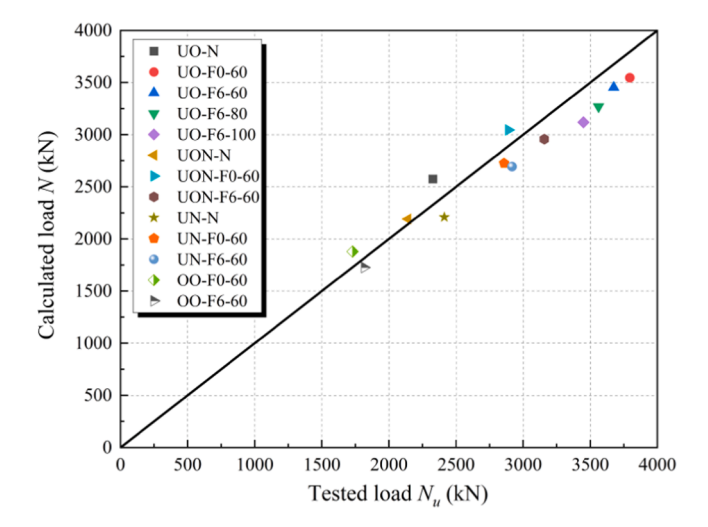


Fig. 13. Calculated vs. Tested values of peak load.

(5) A predictive model for the axial load-bearing capacity of the composite columns demonstrates strong agreement with experimental results, with errors under 10 %.

In summary, this study innovatively proposed a concrete-filled UHPC tubular column reinforced with self-prestressed Fe-SMA spiral stirrup. Through "autoclave curing", the production time was significantly shortened, while the objective of applying prestress to the UHPC tube was successfully achieved. The composite column investigated in this study is well suited for prefabrication and assembly in practical engineering applications. The prestress provided by Fe-SMA stirrups effectively mitigates cracking in the UHPC tube, while the UHPC tube offers superior corrosion protection to the inner concrete core. The composite system has potential applications in fields such as marine engineering and cross-sea bridges in the future.

CRediT authorship contribution statement

Chushi Cui: Writing – original draft, Investigation, Formal analysis, Data curation. Zhiqiang Dong: Writing – review & editing, Supervision, Project administration, Funding acquisition. Yifan Zhao: Writing – review & editing. Tianhao Han: Writing – review & editing. Yichuan Zheng: Writing – review & editing. Writing – review & editing. Elyas Ghafoori: Writing – review & editing.

Declaration of Competing Interest

The authors declare that they have no known competing financial interests or personal relationships that could have appeared to influence the work reported in this paper.

Acknowledgments

The authors would like to acknowledge financial support from the Excellent Youth Foundation of Jiangsu Province of China (BK20230088), the National Natural Science Foundation of China (52378139), National Key Research and Development Program of China (2024YFD1600404–04), the Fundamental Research Funds for the Central Universities (2242022k30031), and the "Zhishan" Scholars Programs of Southeast University.

Data availability

Data will be made available on request.

References

- [1] Zheng Dang, Zhiyuan Li, Peng Feng, Axial compressive behavior of UHPC confined by FRP, Compos. Struct. 300 (2022) 116110, https://doi.org/10.1016/j.
- [2] Caijun Shi, et al., A review on ultra high performance concrete: part I. Raw materials and mixture design, Constr. Build. Mater. 101 (2015) 741–751, https://doi.org/10.1016/j.conbuildmat.2015.10.088.
- [3] Ayan Saha, et al., Assessment of mechanical, durability and microstructural performance of sulphate-resisting cement concrete over portland cement in the presence of salinity, Constr. Build. Mater. 420 (2024) 135527, https://doi.org/10.1016/j.conbuildmat.2024.135527.
- [4] Dehui Wang, et al., A review on ultra high performance concrete: part II. Hydration, microstructure and properties, Constr. Build. Mater. 96 (2015) 368–377, https://doi.org/10.1016/j.conbuildmat.2015.08.095.
- [5] Ali Alsalman, et al., Mixture-proportioning of economical UHPC mixtures, J. Build. Eng. 27 (2020) 100970, https://doi.org/10.1016/j.jobe.2019.100970.
- [6] Junquan Li, et al., Durability of ultra-high performance concrete-A review, Constr. Build. Mater. 255 (2020) 119296, https://doi.org/10.1016/j. conbuildmat 2020 119296
- [7] Hung, Chung-Chan, and Cheng-Hao Yen. "Compressive behavior and strength model of reinforced UHPC short columns." Journal of Building Engineering 35, 2021: 102103. https://doi.org/10.1016/j.jobe.2019.100970..
- [8] Huiwen Tian, et al., Experimental and numerical investigation on the seismic performance of concrete-filled UHPC tubular columns, J. Build. Eng. 43 (2021) 103118, https://doi.org/10.1016/j.jobe.2021.103118.
- [9] Ding, Yi, et al., Compressive behavior of concrete-filled ultra-high performance concrete tube with FRP stirrups, Structures 46 (2022), https://doi.org/10.1016/j.istruc.2022.10.081.
- [10] Gaofei Wang, et al., Compression performance of FRP-steel composite tube-confined ultrahigh-performance concrete (UHPC) columns, Thin-Walled Struct. 192 (2023) 111152, https://doi.org/10.1016/j.tws.2023.111152.
- [11] Huiwen Tian, et al., Experimental investigation on axial compressive behavior of ultra-high performance concrete (UHPC) filled glass FRP tubes, Constr. Build. Mater. 225 (2019) 678–691, https://doi.org/10.1016/j.conbuildmat.2019.07.204.
- [12] Jun-Jie Zeng, et al., Development and behavior of novel FRP-UHPC tubular members, Eng. Struct. 266 (2022) 114540, https://doi.org/10.1016/j.engstruct.2022.114540.
- [13] Jun-Jie Zeng, et al., Novel FRP micro-bar reinforced UHPC permanent formwork for circular columns: concept and compressive behavior, Compos. Struct. 285 (2022) 115268, https://doi.org/10.1016/j.compstruct.2022.115268.
- [14] Sabry Fayed, Walid Mansour, Structural performance of seasand recycled aggregate concrete filled solid/hollow aluminum tubular columns: an experimental work, Structures 47 (2023), https://doi.org/10.1016/j.istruc.2022.12.002.
- [15] Huiwen Tian, et al., Axial behavior of reinforced concrete column with ultra-high performance concrete stay-in-place formwork, Eng. Struct. 210 (2020) 110403, https://doi.org/10.1016/j.engstruct.2020.110403.
- [16] Benjamin Graybeal, Jussara Tanesi, Durability of an ultrahigh-performance concrete, J. Mater. Civ. Eng. 19 (10) (2007) 848–854, https://doi.org/10.1061/(ASCE)0899-1561(2007)19:10(848).
- [17] Cornelia Magureanu, et al., Mechanical properties and durability of ultra-high-performance concrete, Acids Mater. J. 109 (2) (2012), https://doi.org/10.14359/51683704.
- [18] S.M.L.N. Abbas, M.L. Nehdi, M.A. Saleem, Ultra-high performance concrete: Mechanical performance, durability, sustainability and implementation challenges, Int. J. Concr. Struct. Mater. 10 (2016) 271–295, https://doi.org/10.1007/s40069-016-0157-4.
- [19] M.A. Al-Osta, et al., Flexural behavior of reinforced concrete beams strengthened with ultra-high performance fiber reinforced concrete, Constr. Build. Mater. 134 (2017) 279–296, https://doi.org/10.1016/j.conbuildmat.2016.12.094.
- [20] Khan, Muhammad Irfan. Seismic behavior of beam column joints strengthened with ultra high performance concrete. MS thesis. King Fahd University of Petroleum and Minerals (Saudi Arabia), 2017. https://doi.org/10.1016/j.compstruct.2018.05.080.
- [21] Mahsa Farzad, Mohamadreza Shafieifar, Atorod Azizinamini, Retrofitting of bridge columns using UHPC, J. Bridge Eng. 24 (12) (2019) 04019121, https://doi.org/10.1061/(ASCE)BE.1943-5592.0001497.
- [22] Yongming Xiong, et al., Axial compression behavior of concrete-filled prefabricated aligned steel fiber UHPC tubes, J. Build. Eng. 89 (2024) 109353, https://doi.org/10.1016/j.jobe.2024.109353
- [23] Hadi Bahmani, Davood Mostofinejad, Microstructure of ultra-high-performance concrete (UHPC)-a review study, J. Build. Eng. 50 (2022) 104118, https://doi.org/10.1016/j.jobe.2022.104118.
- [24] Serina Ng, et al., Effect of storage and curing conditions at elevated temperatures on aerogel-incorporated mortar samples based on UHPC recipe, Constr. Build. Mater. 106 (2016) 640–649, https://doi.org/10.1016/j.conbuildmat.2015.12.162.
- [25] Jun-Jie Zeng, et al., Durability assessment of ultra-high-performance concrete (UHPC) and FRP grid-reinforced UHPC plates under marine environments, Eng. Struct. 323 (2025) 119313, https://doi.org/10.1016/j.engstruct.2024.119313.
- [26] Safeer Abbas, Ahmed M. Soliman, Moncef L. Nehdi, Exploring mechanical and durability properties of ultra-high performance concrete incorporating various steel fiber lengths and dosages, Constr. Build. Mater. 75 (2015) 429–441, https://doi.org/10.1016/j.conbuildmat.2014.11.017.
- [27] Wei-wen Li, et al., Effects of concrete-stirrup interaction on shear behavior of RC beams under varying shear span-depth ratio scenarios, Structures 61 (2024), https://doi.org/10.1016/j.istruc.2024.106071.
- [28] Yuanxun Zheng, Jingbo Zhuo, Peng Zhang, A review on durability of nano-SiO2 and basalt fiber modified recycled aggregate concrete, Constr. Build. Mater. 304 (2021) 124659, https://doi.org/10.1016/j.conbuildmat.2021.124659.
- [29] Han Zhu, et al., Research on anti-chloride ion penetration property of crumb rubber concrete at different ambient temperatures, Constr. Build. Mater. 189 (2018) 42–53, https://doi.org/10.1016/j.conbuildmat.2018.08.193.
- [30] Jun-Jie Zeng, et al., Behaviour of FRP spiral-confined concrete and contribution of FRP longitudinal bars in FRP-RC columns under axial compression, Eng. Struct. 281 (2023) 115747, https://doi.org/10.1016/j.engstruct.2023.115747.
- [31] Lara Zerbe, et al., Uniaxial compressive behavior of circular concrete columns actively confined with Fe-SMA strips, Eng. Struct. 255 (2022) 113878, https://doi.org/10.1016/j.engstruct.2022.113878.
- [32] Yao Lu, et al., Insights into enhanced shear ductility and toughness of RC beam with fiber reinforced polymer-rubber support composite (FRP-RSC) strengthening system, Eng. Struct. 314 (2024) 118312, https://doi.org/10.1016/j.engstruct.2024.118312.

- [33] Yao Lu, et al., Comparative analysis of shear behavior and mechanism of concrete beams with strip-shaped CFRP or conventional steel stirrups, Case Stud. Constr. Mater. 20 (2024) e03140, https://doi.org/10.1016/j.cscm.2024.e03140.
- [34] X.B. Hu, et al., Behavior of FRP spiral-confined concrete under concentric compression, Eng. Struct. 321 (2024) 118898, https://doi.org/10.1016/j.engstruct 2024 118898
- [35] Wang, Qiang, et al., Axial compressive capacity of RC square columns strengthened by prestressed CFRP with RPC pads, Compos. Struct. 242 (2020) 112153, https://doi.org/10.1016/j.compstruct.2020.112153.
- [36] Lars Janke, et al., Experiments on the residual load-bearing capacity of prestressed confined concrete columns, Eng. Struct. 31 (10) (2009) 2247–2256, https://doi.org/10.1016/j.engstruct.2009.04.006.
- [37] Hasan Moghaddam, et al., Axial compressive behavior of concrete actively confined by metal strips; part A: experimental study, Mater. Struct. 43 (2010) 1369–1381. https://doi.org/10.1617/s11527-010-9588-6.
- [38] Qiang Wang, et al., Experimental study on seismic performance of square RC columns strengthened with multi-layer prestressed CFRP fabric, J. Build. Eng. 45 (2022) 103589, https://doi.org/10.1016/j.jobe.2021.103589.
- [39] Changdong Zhou, Yikun Qiu, Qinglong Pan, Experimental investigation of axial compressive behavior of large-scale circular concrete columns confined by prestressed CFRP strips, J. Struct. Eng. 145 (8) (2019) 04019070, https://doi.org/10.1061/(ASCE)ST.1943-541X.0002351.
- [40] Saidgani Yusufkhojaev, et al., Crack resistance of prestressed reinforced concrete beams with wire rope reinforcement, Materials 16 (19) (2023) 6359, https://doi.org/10.3390/ma16196359.
- [41] Meng Ye, et al., Shear behavior of externally prestressed ultra-high-performance concrete (UHPC) T-beams without stirrups, Eng. Struct. 288 (2023) 116217, https://doi.org/10.1016/j.engstruct.2023.116217.
- [42] Zongcai Deng, et al., Flexural performance of prestressed UHPC beams with different prestressing degrees and levels, Comput. Concr. 34 (4) (2024) 379–391, https://doi.org/10.12989/cac.2024.34.4.379.
- [43] Jianghao Ji, et al., Performance of concrete columns actively strengthened with hoop confinement: A state-of-the-art review, Structures 54 (2023), https://doi.org/10.1016/j.istruc.2023.05.038.
- [44] Zhiqiang Dong, et al., A feasibility study on improving the crack resistance of thin-walled UHPC members by reinforcement with Fe-SMA wires, J. Sustain. Cem. -Based Mater. 14.1 (2025) 103–118. https://doi.org/10.3390/ma16196359.
- [45] Elyas Ghafoori, Bin Wang, Bassem Andrawes, Shape memory alloys for structural engineering: an editorial overview of research and future potentials, Eng. Struct. 273 (2022) 115138, https://doi.org/10.1016/j.engstruct.2022.115138.
- [46] Czaderski, Christoph, et al., Feasibility of iron-based shape memory alloy strips for prestressed strengthening of concrete structures, Constr. Build. Mater. 56 (2014) 94–105, https://doi.org/10.1016/j.conbuildmat.2014.01.069.
- [47] Jakub Vůjtěch, et al., Iron-Based shape memory alloy for strengthening of 113-Year bridge, Eng. Struct. 248 (2021) 113231, https://doi.org/10.1016/j.engstruct.2021.113231.
- [48] Moslem Shahverdi, et al., Iron-based shape memory alloy strips for strengthening RC members: material behavior and characterization, Constr. Build. Mater. 173 (2018) 586–599, https://doi.org/10.1016/j.conbuildmat.2018.04.057.
- [49] Ziqing Liu, et al., Effect of resistive heating on the bond properties between iron-based shape memory bars and cement mortar, J. Build. Eng. 66 (2023) 105895, https://doi.org/10.1016/j.jobe.2023.105895.
- [50] Xinliang Sun, et al., Hinge joint performance in hollow-core slab bridges transversely strengthened with local near-surface mounted iron-based shape memory alloy (Fe-SMA) bars, Constr. Build. Mater. 455 (2024) 139181, https://doi.org/10.1016/j.conbuildmat.2024.139181.
- [51] Ziqing Liu, et al., Experimental investigation on shear behavior of I-shaped concrete beam with Fe-SMA rebars, Eng. Struct. 321 (2024) 119021, https://doi.org/10.1016/j.engstruct.2024.119021.
- [52] Tianhao Han, et al., Axial compression test on strengthening concrete cylinders by Fe-SMA/FRP-HDPE tube and rubber concrete cladding layer, Eng. Struct. 314 (2024) 118380, https://doi.org/10.1016/j.engstruct.2024.118380.
- [53] Jakub Vůjtěch, et al., Strengthening, lifetime extension, and monitoring of a deficient steel–concrete composite roadway bridge using iron-based shape memory alloys, Eng. Struct. 323 (2025) 119286, https://doi.org/10.1016/j.engstruct.2024.119286.
- [54] Ziqing Liu, et al., Mechanical and recovery behavior of a new iron-based shape memory alloy plate, Structures 61 (2024), https://doi.org/10.1016/j.istruc.2024.106049.
- [55] Yichuan Zheng, et al., An activation guideline for the resistive heating process of iron-based shape memory alloy embedded in concrete, Structures 68 (2024), https://doi.org/10.1016/j.istruc.2024.107079.
- [56] Mohammadreza Izadi, Masoud Motavalli, Elyas Ghafoori, Iron-based shape memory alloy (Fe-SMA) for fatigue strengthening of cracked steel bridge connections, Constr. Build. Mater. 227 (2019) 116800, https://doi.org/10.1016/j.conbuildmat.2019.116800.
- [57] E. Ghafoori, et al., Fatigue behavior of a Fe-Mn-Si shape memory alloy used for prestressed strengthening, Mater. Des. 133 (2017) 349–362, https://doi.org/10.1016/j.matdes.2017.07.055.
- [58] Xinliang Sun, et al., Performance of hinge joints in hollow-core slab bridges reinforced with iron-based shape memory alloy U-bars, Structures 70 (2024), https://doi.org/10.1016/j.istruc.2024.107613.
- [59] C.Shawn Sun, et al., Mitigation of end zone cracks in precast prestressed concrete girders using shape memory alloys, Front. Mater. 11 (2024) 1389840, https://doi.org/10.3389/fmats.2024.1389840.
- [60] Lingzhen Li, et al., Analysis and design recommendations for structures strengthened by prestressed bonded Fe-SMA, Eng. Struct. 303 (2024) 117513, https://doi.org/10.1016/j.engstruct.2024.117513.
- [61] Jianghao Ji, et al., Feasibility of using Fe-SMA rebar as cracking resistance spiral stirrup in the anchorage zone of post-tensioned prestressed concrete, Structures 48 (2023), https://doi.org/10.1016/j.istruc.2023.01.011.
- [62] Hongwei Tian, et al., The influence of long-term autoclaving on the properties of ultra-high performance concrete, Front. Mater. 9 (2022) 844268, https://doi.org/10.3389/fmats.2022.844268.
- [63] Sufen Dong, et al., Influence of early thermal curing regimes on properties of ultra-high performance concrete: a review, J. Build. Eng. (2024) 110494, https://doi.org/10.1016/i.jobe.2024.110494.
- [64] Mustafa Azeez Bahedh, Mohd Saleh Jaafar, Ultra high-performance concrete utilizing fly ash as cement replacement under autoclaving technique, Case Stud. Constr. Mater. 9 (2018) e00202, https://doi.org/10.1016/j.cscm.2018.e00202.
- [65] Tiefeng Chen, Xiaojian Gao, Miao Ren, Effects of autoclave curing and fly ash on mechanical properties of ultra-high performance concrete, Constr. Build. Mater. 158 (2018) 864–872, https://doi.org/10.1016/j.conbuildmat.2017.10.074.
- [66] Hongwei Tian, Dietmar Stephan, Christian Lehmann, Mechanical strength and microstructure of ultrahigh-performance concrete under long-term autoclaving, J. Mater. Civ. Eng. 35 (2) (2023) 04022438, https://doi.org/10.1061/(ASCE)MT.1943-5533.0004588.
- [67] Hongru Zhang, et al., Mechanical behavior of ultra-high performance concrete (UHPC) using recycled fine aggregate cured under different conditions and the mechanism based on integrated microstructural parameters, Constr. Build. Mater. 192 (2018) 489–507, https://doi.org/10.1016/j.conbuildmat.2018.10.117.
- [68] Maximilian Schleiting, et al., Potential of Fe-Mn-Al-Ni shape memory alloys for internal prestressing of ultra-high performance concrete, Materials 16 (10) (2023) 3816, https://doi.org/10.3390/ma16103816.
- [69] A. Wetzel, et al., Multifunctional prefabricated walls made of UHPC and foam concrete. Insights and Innovations in Structural Engineering, Mechanics and Computation, CRC Press, 2016, pp. 1375–1379, https://doi.org/10.1201/9781315641645-225.
- [70] GB175-2007, Common Portland Cement, China Architecture and Building Press, Beijing, China, 2007 (In Chinese).
- [71] GB/T 50081-2019. "Standard for test methods of concrete physical and mechanical properties." Ministry of housing and urban-rural development of the People's Republic of China 2019. (In Chinese).
- [72] Tianhao Han, et al., Axial compression test on concrete columns hybrid strengthened with CFRP/CPVC tube and ECC cladding layers, Structures 52 (2023), https://doi.org/10.1016/j.istruc.2023.03.183.

- [73] Chushi Cui, et al., Axial compressive behavior of UHPC columns reinforced with self-prestressed Fe-SMA spiral stirrups, Structures 77 (2025), https://doi.org/ 10.1016/j.istruc.2025.109107.
- [74] Jun-Jie Zeng, et al., Behavior of FRP Ring-Confined CFST columns under axial compression, Compos. Struct. 257 (2021) 113166, https://doi.org/10.1016/j.compstruct.2020.113166.
- [75] Jian C. Lim, Togay Ozbakkaloglu, Influence of silica fume on stress-strain behavior of FRP-confined HSC, Constr. Build. Mater. 63 (2014) 11–24, https://doi.org/10.1016/j.conbuildmat.2014.03.044.
- [76] A.M.T. Hassan, S.W. Jones, G.H. Mahmud, Experimental test methods to determine the uniaxial tensile and compressive behaviour of ultra high performance fibre reinforced concrete (UHPFRC), Constr. Build. Mater. 37 (2012) 874–882, https://doi.org/10.1016/j.conbuildmat.2012.04.030.
- [77] JinJing Liao, et al., FRP-confined concrete columns with a stress reduction-recovery behavior: a state-of-the-art review, design recommendations and model assessments, Compos. Struct. 321 (2023) 117313, https://doi.org/10.1016/j.compstruct.2023.117313.
- [78] JinJing Liao, et al., Compressive behavior of FRP-confined ultra-high performance concrete (UHPC) in circular columns, Eng. Struct. 249 (2021) 113246, https://doi.org/10.1016/j.engstruct.2021.113246.
- [79] JinJing Liao, et al., Design-oriented stress-strain model for FRP-confined ultra-high performance concrete (UHPC), Constr. Build. Mater. 318 (2022) 126200, https://doi.org/10.1016/j.conbuildmat.2021.126200.
- [80] Yeongmo Yeon, Sangwon Ji, Kinam Hong, Uniaxial compressive behavior of concrete column actively confined with internal Fe-SMA spirals, Constr. Build. Mater. 418 (2024) 135393, https://doi.org/10.1016/j.conbuildmat.2024.135393.
- [81] Cao Thanh Ngoc Tran, Bing Li, Ultimate displacement of reinforced concrete columns with light transverse reinforcement, J. Earthq. Eng. 17 (2) (2013) 282–300, https://doi.org/10.1080/13632469.2012.730117.
- [82] John B. Mander, Michael J.N. Priestley, Robert Park, Theoretical stress-strain model for confined concrete, J. Struct. Eng. 114 (8) (1988) 1804–1826, https://doi.org/10.1061/(ASCE)0733-9445(1988)114:8(1804).
- [83] Yi Li, De-Cheng Feng, Gang Wu, Mapping structural damage to material damage for analysis of urban buildings considering actual damage states, J. Build. Eng. (2024) 111356, https://doi.org/10.1016/j.jobe.2024.111356.
- [84] Li, Bing, R. Park, and H. Tanaka. "Stress-strain behavior of high-strength concrete confined by ultra-high-and normal-strength transverse reinforcements." 2001. https://doi.org/10.14359/10228..
- [85] Ali R. Khaloo, H.Ahmad Shuaib, Behavior of high-strength concrete under torsional triaxial compression, Mater. J. 86. 6 (1989) 550–558, https://doi.org/ 10.14359/2194.
- [86] Jian C. Lim, Togay Ozbakkaloglu, Lateral strain-to-axial strain relationship of confined concrete, J. Struct. Eng. 141 (5) (2015) 04014141, https://doi.org/10.1061/(ASCE)ST.1943-541X.0001094.
- [87] D.C. Candappa, J.G. Sanjayan, Sujeeva Setunge, Complete triaxial stress-strain curves of high-strength concrete, J. Mater. Civ. Eng. 13 (3) (2001) 209–215, https://doi.org/10.1061/(ASCE)0899-1561(2001)13:3(209).
- [88] M.A. Tasdemir, et al., Evaluation of strains at peak stresses in concrete: a three-phase composite model approach, Cem. Concr. Compos. 20 (4) (1998) 301–318, https://doi.org/10.1016/S0958-9465(98)00012-2.